12th International Symposium on Turbulence and Shear Flow Phenomena (TSFP12)
Osaka, Japan, July 19–22, 2022

MODELLING SECONDARY STRUCTURES DEVELOPING OVER LONGITUDINAL RIDGES WITH DIFFERENT GEOMETRIES

Gerardo Zampino, Davide Lasagna, Bharath Ganapathisubramani
Aeronautics and Astronautics
Faculty of Engineering and Physical Sciences
University of Southampton,
Southampton, SO17 1BJ, UK
g.zampino@soton.ac.uk

INTRODUCTION

Secondary flows are generated when a lateral variation of the topography, such as streamwise aligned ridges, is imposed to a turbulent wall-bounded flow. In this case, the flow field is characterized by vortical structures developing along the streamwise direction known as Prandt's vortices of the second kind (Prandtl, 1952). These surfaces have gained increasing importance in industrial applications because secondary flows alter and modify the performances of fluid dynamics surfaces (Jiménez, 2004; Mejia-Alvarez & Christensen, 2013). It has been shown that the flow organization and the strength of such structures can depend on the shape of the ridges (Medjnoun *et al.*, 2020) but how the geometry affects the generation mechanism of secondary structures and their strength is not fully clear. Some authors (Wu & Christensen, 2007; Castro *et al.*, 2021) observed that, in some cases, secondary flows over different geometries appear to be similar and this suggests a possible scaling of the vortical structures with a geometrical property of the surface. In particular, Castro *et al.* (2021) concluded that the strength of the secondary flows developing over rectangular ridges depends on the ratio between the ridge spacing and width and the flow organization is independent of the spacing when scaled with the channel height. Other scaling geometrical parameters have been proposed in literature, such as the ratio between the wetted area above and below the ridge mean height by Medjnoun *et al.* (2020). In this paper, we address these questions by developing a tool based on linearized Reynolds-Averaged Navier-Stokes (RANS) equations with the Spalart-Allmaras (SA) turbulence model to close the system. To contrast and compare the most common studied ridge geometries, we apply the present tool to elliptical, triangular and rectangular ridges.

LINEARIZED RANS EQUATIONS

A pressure-driven channel with streamwise aligned ridges is studied. A symmetric channel configuration is here considered. In the following, the streamwise, wall-normal and spanwise directions, normalized with the channel half height h, are identified by the cartesian coordinates (x_1, x_2, x_3) respectively. The coordinate system is centred on the channel mid-plane.

The flow is governed by the Reynolds-Averaged continuity and the momentum equations for the velocity components (u_1, u_2, u_3) scaled with the friction velocity u_τ. The one-equation SA turbulence model (Spalart & Allmaras, 1994) is used as closure model for the eddy viscosity ν_t. A sketch of the ridge geometries considered is reported in figure 1(a,b,c), where S is the spacing between the ridges and W is the ridge width. The entire methodology is based on decomposing the flow field into a homogeneous flow over the flat channel and the flow perturbation induced by the ridges. Defining ε as the peak-to-peak distance of the ridge, we expand any time-averaged flow quantity q using a Taylor series in ε as

$$q(x_2, x_3) = q^{(0)}(x_2) + \varepsilon q^{(1)}(x_2, x_3) + \mathscr{O}(\varepsilon^2), \tag{1}$$

where the zero-order term $q^{(0)}$ is the base flow solution in the flat channel and the first-order term $q^{(1)}$ is the flow response per unit of ridge height. Following Russo & Luchini (2016), in the limit of small ridges, we assume that the intensity of the secondary currents is proportional to ε. Thus, in the definition (1) higher order terms in ε are neglected. For streamwise aligned ridges, we consider a streamwise invariant flow, thus $\partial \cdot / \partial x_1 = 0$. Substituting the Taylor expansion (1) in the governing equations written using the streamwise velocity u_1 and streamfunction ψ formulation, and considering the terms at order one in ε, we obtain

$$-\frac{\partial \psi^{(1)}}{\partial x_3}\Gamma = \frac{1}{Re_\tau}\left(\frac{\partial^2}{\partial x_2^2} + \frac{\partial^2}{\partial x_3^2}\right) u_1^{(1)} + \frac{\partial \tau_{12}^{(1)}}{\partial x_2} + \frac{\partial \tau_{13}^{(1)}}{\partial x_3}, \tag{2}$$

$$\begin{aligned} 0 = {} & \frac{1}{Re_\tau}\left(\frac{\partial^2}{\partial x_2^2} + \frac{\partial^2}{\partial x_3^2}\right)^2 \psi^{(1)} \\ & + \frac{\partial^2}{\partial x_2 \partial x_3}\left(\tau_{33}^{(1)} - \tau_{22}^{(1)}\right) + \left(\frac{\partial^2}{\partial x_2^2} - \frac{\partial^2}{\partial x_3^2}\right)\tau_{23}^{(1)}, \end{aligned} \tag{3}$$

where Γ is the zero-order streamwise velocity wall-normal gradient, $Re_\tau = u_\tau h/\nu$ is the friction Reynolds number and $\tau_{ij}^{(1)}$ is the Reynolds stress tensor perturbation. Similarly, to close the system of equations (2) and (3), the SA transport equation for the perturbation of the eddy viscosity $\nu_t^{(1)}$ induced by the ridges is linearized (here omitted for brevity).

The tensor $\tau_{ij}^{(1)}$ must be expressed as a function of $\nu_t^{(1)}$ and the other mean quantities. As already discussed in literature of noncircular ducts (Perkins, 1970; Bottaro *et al.*, 2006), when the linear Boussinesq's hypothesis is used, no secondary flows can be predicted because the streamwise momentum equation (2) and the streamfunction equation (3) are decoupled. Hence, a nonlinear Reynolds stress model is necessary

for the correct prediction of anisotropic stresses that are the source of the secondary flows. In order to have a compact and simple model to be manipulated, the Quadratic Constitutive Relation (QCR) nonlinear stress model (Spalart, 2000) is here integrated in the SA turbulence model. The Reynolds stresses become

$$\tau_{ij} = \tau^L_{ij} - C_{r1}\left[O_{ik}\tau^L_{jk} + O_{jk}\tau^L_{ik}\right], \tag{4}$$

where O_{ik} is the normalized rotation tensor and $\tau^L_{ij} = \nu_t S_{ij}$ is the linear Reynolds stress tensor from the Boussinesq's approximation with S_{ij} the mean velocity gradient tensor. The constant $C_{r1} = 0.3$ is calibrated to match the anisotropy in the outer region over wall-bounded turbulent flows following Spalart (2000).

The effect of the ridges is introduced using linearized boundary conditions (Luchini, 2013; Busse & Sandham, 2012). Expanding the velocity near the surface in a Taylor series in x_2 and enforcing the no-slip condition at the physical surface, the streamwise velocity component at the lower domain boundary is given by the inhomogeneous boundary condition

$$u_i^{(1)}\Big|_{x_2=-1} + f(x_3)\left.\frac{\partial u_i^{(0)}}{\partial x_2}\right|_{x_2=-1} = 0, \tag{5}$$

i.e. the perturbation velocity at the boundary of the numerical domain is proportional to the wall-normal gradient of the velocity in the plane channel to preserve the no-slip condition on the modulated topography. Similarly, inhomogeneous boundary conditions are derived for the perturbation eddy viscosity $\nu_t^{(1)}$ which vanishes at the physical surface. Finally, any periodic wall modulation with an unitary ridge height is modelled by the zero-mean modulation

$$f(x_3) = \sum_{n=1}^{\infty} f^n \cos(nk_3x_3), \tag{6}$$

where f^n is the amplitude of the n-th wavenumber mode and $k_3 = 2\pi/S$ is the fundamental wavenumber. The flow field over any complex geometry can be reconstructed following the superposition principle. Since the first-order equations are linear, a complex solution is given by the constructive (or destructive) interference of solutions at independent wavenumbers. The entire methodology is extensively described in Zampino *et al.* (2022).

RESULTS

Linear prediction of flow organization

Secondary flows are predicted over elliptical, rectangular and triangular ridges at $Re_\tau = 1000$ for duty cycle $DC = W/S = 0.5$ and $W = 0.25$ (left panels), 0.5 (central panels) and 1.0 (right panels) in figure 1. The contour lines of the perturbation streamfunction $\psi^{(1)}$ and the colour map of the wall-normal velocity perturbation $u_2^{(1)}$ are also reported to better display the flow organization. Because symmetric channel configurations are studied, subjected to a periodic wall modulation, only the bottom half-channel and a single ridge period is here shown. For small spacing (left column), vortical structures predicted for all three geometries show an upwelling (downwelling) motion above the ridges (inside the troughs). The secondary vortices occypy only a quarter of the channel height and they are similar in size and strength for all three geometries considered. Although some differences are predicted in the very near-wall region where the ridge geometry affects the local flow organization, these differences are weak and negligible. For increasing ridge width, the vortices grow in size and strength until they occupy the entire channel half-height (central column). Some differences are here evident in the strength of secondary flows and stronger downwash velocity is predicted at the gap centre for rectangular ridges. For $W = 1$, very large turbulent structures are observed for all geometries (right panels). In particular, for rectangular ridges, the secondary flows are locked at the ridge edge due to the strong discontinuity introduced by the ridge geometry. The same aspect is also observed for elliptical ridges where the secondary flows develop in proximity of the ridge edge. By contrast, for triangular ridges, the secondary currents occur at the flank of the ridge. For this case, tertiary flows at the centre of the trough are predicted only for triangular ridges, and produce a local change of the flow direction. For specific spacings and widths, tertiary flows can also be observed at the centre of the trough for the other geometries when the gap between the ridges is large enough to allow the turbulent structures to fully develop. In fact, for large spacing, the vortical structures reach their maximum size and a further increase of the spacing allows tertiary flows to emerge.

For similar reasons, tertiary flows can be predicted over the ridges when the ridge width is large enough. This only occurs for rectangular and elliptical ridges, because of the sharp discontinuity in the height of the ridge topography. By contrast, no tertiary flows over the ridge are observed for the triangular shape because the deflection of the spanwise velocity component induced by the flank of the ridges is weaker.

Studies not reported here show that the Reynolds number affects only the strength of the secondary flows but the flow organization is unaffected. More specifically, for high Reynolds number, the solution of the present model becomes Reynolds invariant because of the turbulence model used. In fact, the Spalart-Allmaras model (Spalart & Allmaras, 1994) is built in order to obtain a collapse of the eddy viscosity profile in the logarithmic layer for high Reynolds numbers. As a consequence, the eddy viscosity profile and the Reynolds stresses are asymptotically Reynolds number independent when scaled with the friction velocity. For this reason, the results for $Re_\tau = 1000$ were here reported and they are representative of the secondary flows generated by the ridges also at high Reynolds numbers.

Scaling of the dispersive stresses

In many experimental and numerical works, dispersive stresses

$$\sigma_{ij}(x_2,x_3) = u_i^{(1)}(x_2,x_3)u_j^{(1)}(x_2,x_3)$$

are commonly used to study the generation of secondary flows. In order to characterize their global strength using a single scalar quantity, we introduce the integral

$$R^l_{ij} = \int_0^S \int_{-l}^{l} \sigma_{ij}(x_2,x_3)\mathrm{d}x_2\mathrm{d}x_3, \tag{7}$$

where we take $l = 0.9$ to discard the contribution in the near-wall region. The map of $R^{0.9}_{12}$ is plotted in the panels (d,e,f)

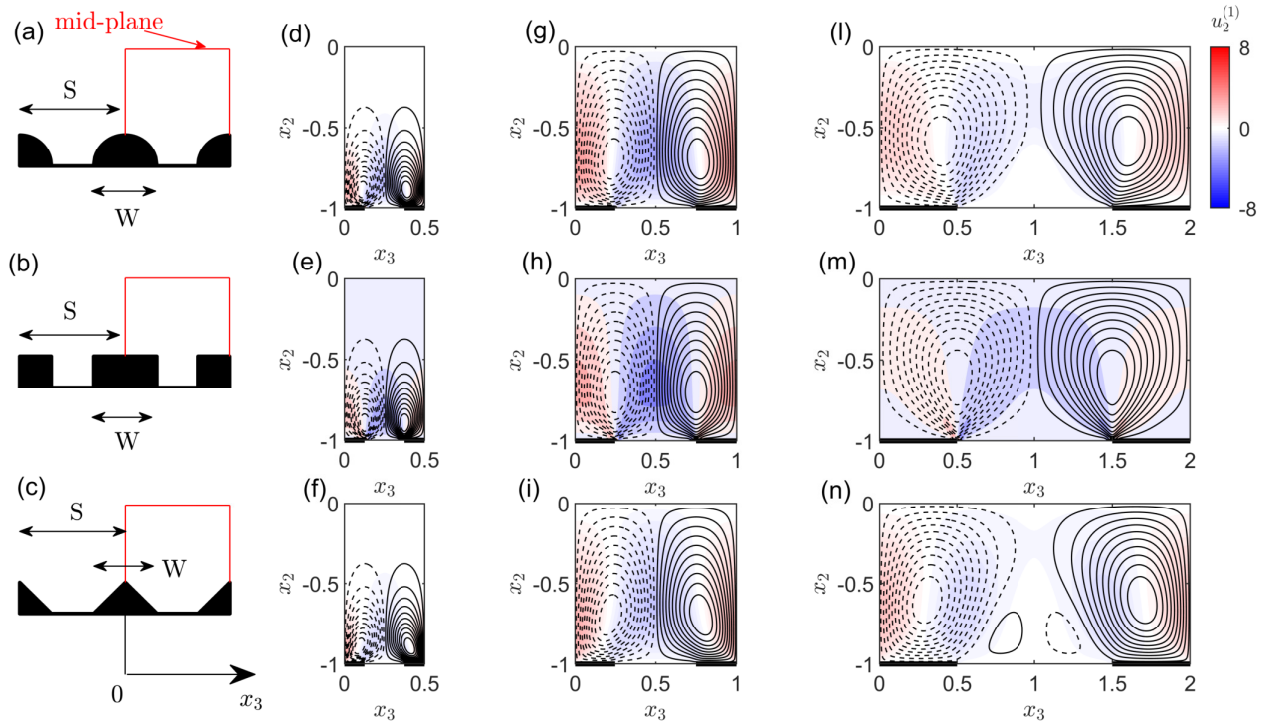

Figure 1. Contour lines of the perturbation streamfunction $\psi^{(1)}$ at $Re_\tau = 1000$ and for elliptical ridges (top panels), rectangular ridges (central panels) and triangular ridges (bottom panels). Dashed lines are used for negative values. A sketch of the cases studied is reported in panels (a,b,c). The flow organization is shown for the bottom half channels in the region delimited by the red lines. The colour map of the wall-normal velocity perturbation $u_2^{(1)}$ is also reported to better display the flow organization above the ridges. The duty cycle $DC = 0.5$ for all cases while the width varies from 0.25 (left column) 0.5 (central column) and 1 (right column). To help the reader, a simplified representation of the ridges is reported at the bottom of each plot (bold black lines).

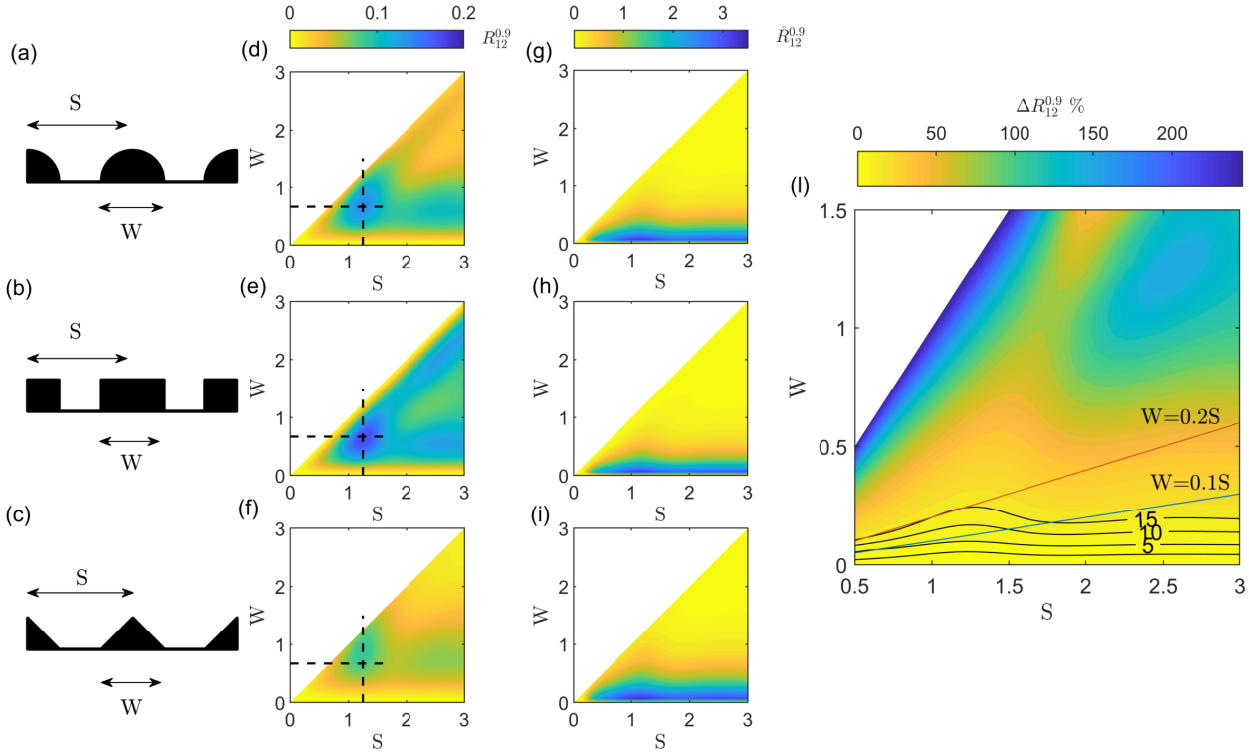

Figure 2. Integral dispersive stress $R_{12}^{0.9}$ (d,e,f) and scaled dispersive stress $\hat{R}_{12}^{0.9}$ (g,h,i) are reported as a function of the ridge spacing S and ridge width W for $Re_\tau = 1000$ for elliptical ridges (top panels), rectangular ridges (central panels) and triangular ridges (bottom panels). The dashed lines identify the peak amplification configuration at $(S,W) = (1.25, 0.67)$ A sketch of the cases studied is reported in panels (a,b,c). The quantity $\Delta\hat{R}_{12}^{0.9}$ is reported in panel (l) where the black contours are plotted for $\Delta\hat{R}_{12}^{0.9}\% = 2, 5, 10$ and 15%. The straight lines for $W = 0.1S$ (blue) and $W = 0.2S$ (red) are also shown.

of figure 2 for $Re_\tau = 1000$ and as a function of S and W. For all cases studied, we predict i) a region of high amplification at $(S,W) \approx (1.25, 0.67)$, denoted by the intersection of the dashed lines, where the strength of the secondary flows is maximum, and ii) high amplification along a line at constant $W \approx 0.67$. However, the peak values across the three cases are different (stronger for rectangular ridges), confirming that the strength of secondary currents depends on the ridge geometry. For high spacing S or width W, the quantity $R_{12}^{0.9}$ for rectangular ridges also displays a second amplification peak not visible for the other geometries and corresponding to the maximum strength of the tertiary flows developing at the ridge centre (or trough centre).

Despite the difference in the strength of the response, the flow organization observed for the narrow ridge case $W = 0.2$ shown in figure 1 is similar for all geometries, suggesting that the cross-stream velocities and dispersive stresses might be scaled using an appropriate geometrical parameter. In this particular regime, one can assume that the surface perturbation generating the secondary currents is localised in a narrow region at the wall and the effect of the ridge is proportional to its cross-sectional area but not its geometry. For this reason, we introduce the mean ridge height $\overline{H}$ as the ratio between the cross-sectional area and the spacing S and use this quantity to scale the perturbation velocity field. In addition, since the dispersive stresses are given by the product of the velocity perturbations, the quantity $R_{12}^{0.9}$ is scaled with the square of the mean ridge height $\overline{H}$. Maps of $\hat{R}_{12}^{0.9} = R_{12}^{0.9}/\overline{H}^2$ obtained for the three geometries are plotted in panels (g,h,i) of figure 2 as a function of the spacing S and the ridge width W. These maps show strong similarities for the region characterized by high ratio S/W *and* small W. We define these two areas of the parameter space as the "isolated ridge" regime, where ridges are small in width compared to the distance from one another, and the "narrow ridge" regime, where the ridge is narrow compared to the boundary layer thickness. To better visualise this behaviour, we introduce the quantity

$$\Delta\hat{R}_{12}^{0.9}\% = \frac{\max \hat{R}_{12}^{0.9} - \min \hat{R}_{12}^{0.9}}{\text{mean}\, \hat{R}_{12}^{0.9}} \cdot 100, \tag{8}$$

where the function "max" is the maximum value obtained across the three geometries for a fixed configuration (S,W). Similarly, we define the functions "min" and "mean" as the minimum and the mean value, respectively. The quantity $\Delta\hat{R}_{12}^{0.9}\%$ can be interpreted as the difference in secondary flows strength across the three geometries for the same width and spacing. This quantity is plotted in figure 2(l) where selected contours are reported for the difference of $2, 5, 10$ and 15%, to ease the visualisation. We can observe that the relative difference in scaled strength is small if the ridges are either narrow or isolated. If this condition is not met, for configurations where the ridges are wide or tightly packed, the difference in the scaled dispersive stresses across the three geometries increases.

Flow organization and scaling behaviour

In order to compare the flow response for the ridge configurations showing a scaling behaviour of the secondary flows and the configurations where it does not hold, the contours of the streamfunction $\psi^{(1)}$ and the map of the scaled wall-normal velocity $u_2^{(1)}/\overline{H}$ are reported in figure 3. Two configurations are here considered: $(S,W) = (1.25, 0.2)$ where $\Delta\hat{R}_{12}^{0.9}\% \approx 15\%$ (top panels) and $(S,W) = (2,1)$ where $\Delta\hat{R}_{12}^{0.9}\% \approx 150\%$ (bottom panels).

For the first configuration, we predict two counter-rotating vortices that occupy the entire half-height of the channel. The fact that the flow organization is similar for all geometries for regimes where the ridges are narrow *and* isolated explains why the strength of secondary flows can be scaled with the mean ridge height. If the ridge is wide *or* tightly packed, for $(S,W) = (2,1)$ (bottom panels), the flow topology depends on the ridge shape and scaling the velocity components with the ridge mean height does not lead to a collapse of the response. Generally, an upwash (downwash) is predicted at the centre of the ridge (trough) for the three ridge geometries but this is not sufficient to produce a scaling of the secondary flows. The position and the orientation of the vortices are different.

Velocity profiles

For a better characterization of the scaling of the secondary flows, the velocity components profiles divided by $\overline{H}$ for elliptical, triangular and rectangular ridges are reported in figure 4. Three cases are here considered for a constant spacing $S = 1.25$ and varying width in order to display the scaling behaviour for narrow *and* isolated ridges for $W = 0.2$ (left column), and the scaling breakdown for $W = 0.67$ (central column), corresponding to the maximum amplification configuration, and for $W = 1.0$ (right column), corresponding to wide ridges. The wall-normal velocity profiles for the three geometries at the ridge centre and at the centre of the trough are reported in the top and central panels, respectively. The spanwise velocity component at the ridge edge is also provided in the bottom panels. The wall-normal velocity $u_2^{(1)}/\overline{H}$ at the ridge centre (top panels) collapses in the far-wall region only for $W = 0.2$ whereas for increasing ridge width the scaled profiles differ and no collapsing is observed. Close to the wall (panel a), the velocity profiles show a peak value that depend on the ridge geometry. This is due to the proximity to the ridge that locally modify the flow field. For increasing width (panel b and c), the velocity profiles differ. The ridge geometry affects the peak value (higher for triangular ridges). For increasing W, the strength of the vortices decreases, too.

Similarly, the wall-normal velocity at the centre of the trough is plotted in panels (d,e,f) of figure 4. These velocity profiles collapse for the entire channel height only for the isolated ridge configuration ($W = 0.2$). To explain the collapse of the profiles at the centre of the trough for narrow *and* isolated ridges, one can observe that the secondary flows at the centre of the trough are not affected by the ridge geometry, since the distance from the nearest ridge is large compared with W. The peak value slightly changes for $W = 0.67$. For $W = 1.0$ where the gap is reduced, the velocity profiles are strongly dependent on the ridge geometry and its effect is not negligible when moving towards the centre of the channel. However, a collapse of the curves is still observed in the near wall region where the influence of the ridges is weak.

For all three geometries and for $W = 0.2$, the spanwise velocity profiles in the bottom panels collapse along the entire wall-normal direction. A negative peak is predicted at the wall over the ridge edge where the Reynolds stresses are stronger. Except for the case $W = 0.2$, the peak value depends on the ridge geometry. Moving towards the channel centre, the velocity decreases in magnitude. For increasing width, the scaling breaks down and some differences can be observed across the three geometries.

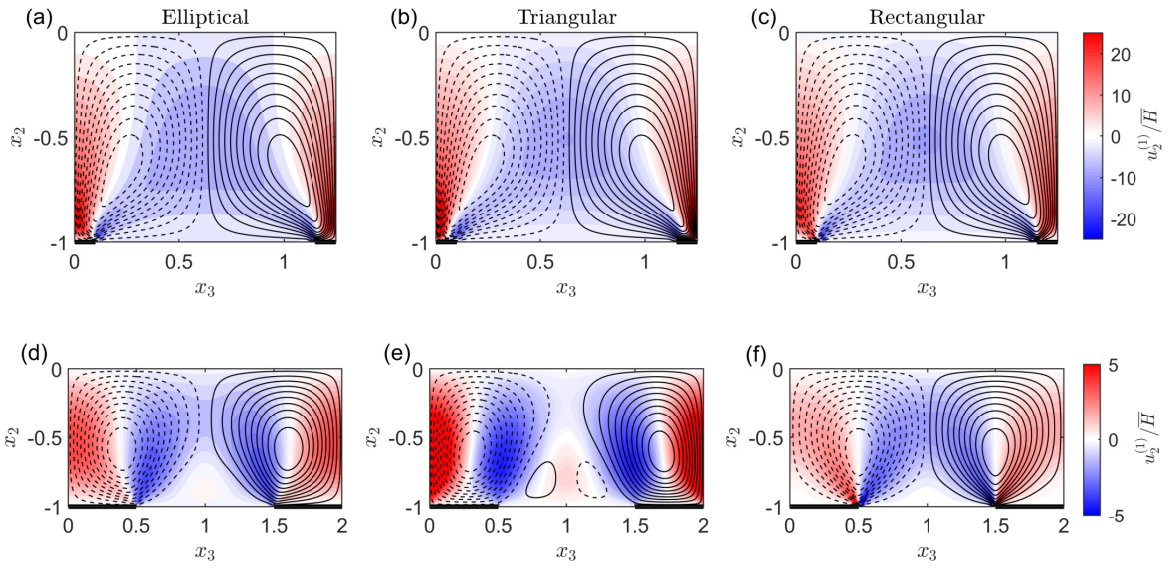

Figure 3. Colour maps of the wall-normal velocity $u_2^{(1)}$ scaled with $\overline{H}$ for elliptical, triangular and rectangular ridges. The Reynolds number is $Re_\tau = 1000$ for $(S,W) = (1.25, 0.2)$ (top panels) and $(S,W) = (2,1)$ (bottom panels). The contour To help the reader, a simplified representation of the ridges is reported at the bottom of each plot (bold black lines). The black lines are the contours of constant streamfunction $\psi^{(1)}$ (solid lines for positive values and dashed lines for negative values).

CONCLUSIONS

The present approach provides an approximation of secondary flows produced by different ridge geometries using a linearized RANS based model. The model allows to quickly predict the flow organization over a large variety of different ridge configurations, at a reduced computational cost. Here, secondary flows over elliptical, triangular and rectangular ridges are investigated. We assume that any flow quantity can be decomposed as a zero-order and a first-order term corresponding to the flow perturbation generated by the ridges. In the limit of small ridges, linearized equations are obtained for the perturbation of the streamwise velocity u_1 and the streamfunction ψ and they are solved by imposing inhomogeneous boundary conditions to model the effect of the ridges. Since the equations are linear, the superposition principle is applied to reconstuct the flow field over complex geometries. Results for $Re_\tau = 1000$ are reported as a representative case.

The flow organization is displayed for the three geometries. Strong similarities in size of the secondary flows are observed for narrow ridges with small width compared with the spacing. For increasing width, the vortices grow in strength and size until they entirely occupy the half channel height. The flow organization differs and for wide ridges where the secondary structures depend on the ridge geometry.

These similarities in the flow topology for narrow ridges suggest that secondary structures can be scaled using an appropriate parameter that depends on the ridge geometry. Since the ridges are localized at the wall, the effect of the wall perturbation is assumed to be proportional to the cross-sectional area of the ridges not their geometry. For this reason, the mean ridge height $\overline{H}$ is here proposed as the scaling parameter.

The integral of the dispersive stresses are here used to characterize the strength of secondary flows with a single scalar quantity. The maps of $R_{12}^{0,9}$ are are scaled with $\overline{H}^2$ and they collapse for the ridge configurations with small width W, defining the "narrow ridges" regime, *and* high ratio S/W, defining the "isolated ridges" regime. For these configurations the effect of the ridge geometry is negligible or confined to the very near-wall region and the scaled velocity profiles collapse. Finally, the scaled velocity components profiles for different configurations are also compared. The velocity profiles collapse only for the case corresponding to narrow *and* isolated ridges. In particular, the collapse of the profiles at the centre of the trough can be easily explained as the consequence of the low influence of the nearest ridge. For increasing width, the scaling behaviour breaks down because the flow topology strongly depends on the ridge geometry.

REFERENCES

Bottaro, A., Soueid, H. & Galletti, B. 2006 Formation of secondary vortices in turbulent square-duct flow. *AIAA Journal* **44**, 803–811.

Busse, A. & Sandham, N. D. 2012 Influence of an anisotropic slip-length boundary condition on turbulent channel flow. *Phys. Fluid* **24**, 055111.

Castro, I. P, Kim, J. W., Stroh, A. & Lim, H. C. 2021 Channel flow with large longitudinal ribs. *J. Fluid. Mech.* **915**, A92.

Jiménez, J. 2004 Turbulent flows over rough walls. *Annu. Rev. Fluid Mech.* **36**, 173–196.

Luchini, P. 2013 Linearized no-slip boundary conditions at rough surface. *J. Fluid Mech.* **737**, 349–367.

Medjnoun, T., Vanderwel, C. & Ganapathisubramani, B. 2020 Effects of heterogeneous surface geometry on secondary flows in turbulent boundary layers. *J. Fluid Mech.* **886**, A31.

Mejia-Alvarez, R. & Christensen, K. 2013 Wall-parallel stereo particle-image velocimetry measurements in the roughness sublayer of turbulent flow overlying highly irregular roughness. *Phy. Fluids* **25**, 115109.

Perkins, H. J. 1970 The formation of streamwise vorticity in turbulent flow. *J. Fluid Mech.* **44**, 721–740.

Prandtl, L. 1952 *Essentials of fluid dynamics*. Hafner.

Russo, S. & Luchini, P. 2016 The linear response of turbulent

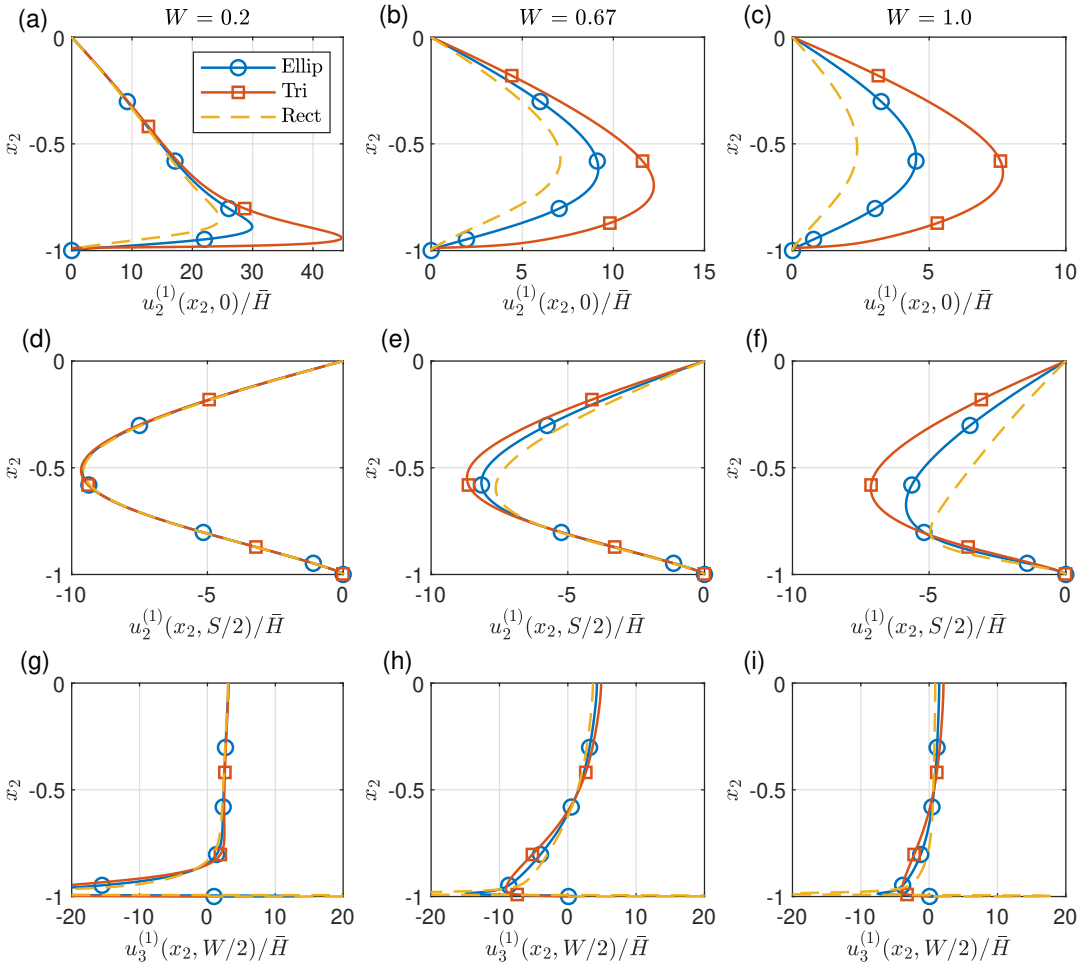

Figure 4. Scaled profiles of the wall-normal velocity component at the centre of the ridge (top panels) and at the centre of the gap (central panels). The spanwise velocity component is extrapolated at the ridge edge (bottom panels). The spacing is $S = 1.25$ and the ridge width $W = 0.2$ (left column), 0.67 (central column) and 1.0 (right column). The profiles are obtained for the elliptical "Ellip", triangular "Tri" and rectangular "Rect" ridges for $Re_\tau = 1000$.

flow to a volume force: comparison between eddy-viscosity model and dns. *J. Fluid Mech.* **790**, 104–127.

Spalart, P. R. 2000 Strategies for turbulence modelling and simulations. *Int. J. Heat Fluid Flow* **21**, 252–263.

Spalart, P. R. & Allmaras, S. R. 1994 A one-equation turbulence model for aerodynamic flows. *Rech. Aerosp.* **1**, 5–21.

Wu, Y. & Christensen, K. T. 2007 Outer-layer similarity in the presence of a practical rough-wall topography. *Phys. Fluid* **19**, 085108.

Zampino, G., Lasagna, D. & Ganapathisubramani, B. 2022 Linearised reynolds-averaged predictions of secondary currents in turbulent channels with topographic heterogeneity. arXiv:2111.08459.